Published in "Physical Review A: Atomic, Molecular and Optical Physics 76(2): 022502, 2007" which should be cited to refer to this work.

$6S_{1/2}$-$6P_{1/2}$ transition of Cs atoms in cubic and hexagonal solid ^{4}He

A. Hofer,* P. Moroshkin, S. Ulzega,† D. Nettels,‡ R. Müller-Siebert,§ and A. Weis
Département de Physique, Université de Fribourg, Chemin du Musée 3, 1700 Fribourg, Switzerland‖

We present a systematic experimental study of the absorption and fluorescence spectra of the $6S_{1/2}$-$6P_{1/2}$ transition in Cs atoms isolated in solid ^{4}He matrices. The bubble model developed earlier for alkali-metal atoms in liquid He is revised and applied to the present system. The analysis of the dependencies of absorption and fluorescence wavelengths on He pressure in liquid and solid He (cubic and hexagonal) environments leads us to modify the bubble model by taking the elastic deformation of solid He by the atomic bubble into account.

PACS number(s): 32.30.−r, 32.70.Jz, 33.20.Ea, 67.40.Yv

I. INTRODUCTION

Alkali-metal atoms implanted in condensed He reside in nanosize spherical cavities—so-called atomic bubbles. These bubbles are formed around each impurity atom due to the Pauli principle that forbids any overlap between the closed S shells of He atoms and the valence electron of the impurity. In the ground state of alkali-metal atoms the valence electron is loosely bound in a spherically symmetric $nS_{1/2}$ orbital and the bubble is similar, albeit smaller, than that of a free electron in condensed helium. The spectroscopy of electrons in liquid [1,2] and solid [3] He has been developed in the early 1990s and the experimental results confirmed the predictions of the bubble model. Already in those studies it was found that the model originally developed for liquid He produces reliable results also for solid He—a consequence of the quantum nature of He crystals, where the He atoms are strongly delocalized. A similar tendency was observed in studies of absorption and emission spectra of alkali-metal atoms (Cs and Rb) in liquid [4,5] and solid [6] He, as well as for Ba atoms [7,8]. However, a more detailed analysis [9] of the spectral shift of the $6S_{1/2}$-$6P_{1/2}$ (D_1) transition of Cs atoms in He matrices as a function of He pressure reveals relatively large abrupt changes at the phase boundaries, which cannot be predicted by the bubble model.

A theoretical investigation of bubbles formed by Cs and Rb atoms in pressurized liquid He has been performed in [4,5] and its results demonstrated a good agreement with experimental results. In the present paper we report on the results of systematic experimental investigations of the D_1 transition of Cs in solid He in a broad range of pressures, covering the body-centered cubic (bcc) and the hexagonal close-packed (hcp) crystalline phases. We also revise the bubble model and apply it to Cs atoms in solid He. We have included several effects not considered in the previous theoretical treatment of [4] (i) the modification of the fine-structure splitting of Cs by the interaction with He; (ii) the interaction of the atomic dipole with its own radiation reflected at the bubble interface. We have further identified a contribution to the bubble energy due to elastic crystal deformations, which is not present in the case of liquid He, but which should be taken into account in solid He. The extended bubble model has allowed us to calculate absorption and emission spectra, which are in good agreement with the experimental results obtained in liquid and solid He. We have applied our model calculations to the fine structure, the lifetime of the excited $6P_{1/2}$ state, and the hyperfine splitting in the ground state of Cs in solid He and compare the results with experimental findings.

II. THEORETICAL MODEL

A. Spherical bubble model

Our approach follows closely the one described in [4]. The essential feature of the standard bubble model (SBM) is the representation of the He matrix as a continuous medium, characterized by its density ρ and surface tension parameter σ. This treatment is justified not only for liquid, but also for solid He, which is a quantum crystal with a very large delocalization of the He atoms, and hence a strong overlap of their wave functions. The solid He matrix is so soft that the impurity atom imposes its own symmetry on the local trapping site. In particular, the spherically symmetric $6S_{1/2}$ and $6P_{1/2}$ electronic states of Cs in the cubic phase of solid He form bubbles of spherical shape.

Following the ideas of [10,11] the many-body problem of the interaction of an alkali-metal atom with a He atom can be reduced to a three-body problem by assuming that the perturbations of the alkali-metal core and the He atom are small compared to the perturbations of the alkali-metal valence electron. We further use the fact that the alkali-metal core and the He atom have closed shell structures. Details of these structures are not considered, but we assume that both can be polarized by the alkali-metal valence electron. The properties of the atomic defect structure can then be described in terms of the mutual interactions of the valence electron, the "frozen" alkali-metal core and the He atom(s). Using the Born-Oppenheimer approximation, the nucleus of the Cs and the He atom(s) can be treated as fixed in space and the problem is reduced to calculating the wave function of the valence electron in the combined potentials that it experiences. The geometry of the problem is sketched in Fig. 1.

*adrian.hofer@unifr.ch
†Now at EPFL, Lausanne, Switzerland.
‡Now at Biochemisches Institut, Universität Zürich, Switzerland.
§Now at SELFRAG AG, Langenthal, Switzerland.
‖www.unifr.ch/physics/frap/

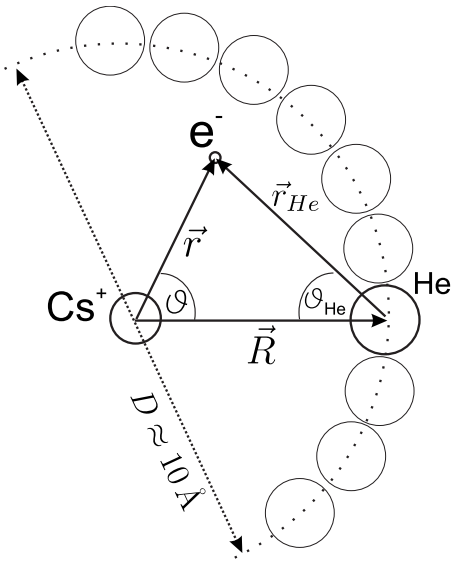

FIG. 1. Schematic model of a Cs atom inside a spherical He bubble. The interaction is treated as a three-body interaction between the Cs^+ core in the center of the bubble (origin of coordinate system), the valence electron of the Cs atom at position $\vec{r}$, and the He atom at position $\vec{R}$. The diameter of the bubble is approximately 1 nm for a ground state Cs atom.

The total potential felt by the alkali-metal valence electron can be written as

$$V_{\rm tot}(\mathbf{r},\mathbf{R}) = V_{\rm Cs}(\mathbf{r}) + V_{\rm He}(\mathbf{r},\mathbf{R}) + V_{\rm cross}(\mathbf{r},\mathbf{R}) + V_{\rm cc}(\mathbf{R}), \tag{1}$$

where $V_{\rm Cs}(\mathbf{r})$ and $V_{\rm He}(\mathbf{r},\mathbf{R})$ describe the interaction of the electron with the Cs core and the He atom, respectively. The cross term $V_{\rm cross}(\mathbf{r},\mathbf{R})$ describes the three-body interaction, i.e., the polarization of the He atom by the Cs valence electron and the Cs^+ ion. Finally, the last term in Eq. (1), $V_{\rm cc}(\mathbf{R})$, is the core-core interaction of the Cs^+ ion with the ground state He atom.

B. Energy of the free Cs atom

The first term of Eq. (1) has the following contributions:

$$V_{\rm Cs}(r) = V_{\rm TF}(r,\lambda) + V_{\rm pol}(r,r_c) + V_{\rm so}(r), \tag{2}$$

where $V_{\rm TF}(r,\lambda)$ is a scaled statistical Thomas-Fermi model potential. The core polarization due to the valence electron is represented by $V_{\rm pol}(r,r_c)$ and $V_{\rm so}(r)$ is the spin-orbit potential. For systems with many electrons an explicit calculation of the potential is not possible and one has to rely on approximative methods, of which the relativistic Hartree-Fock method has proven to be very successful. Hartree-Fock calculations are beyond our capabilities and we have opted for a simpler approach by using a scaled Thomas-Fermi model potential [12,13] following the work of Norcross [14] to describe the interaction of the Cs valence electron with the Cs core. We have taken the Fermi-Amaldi correction for excluding the electrostatic self-energy of the electron and the exchange energy correction introduced by Dirac into account as described in [12]. This yields a corrected Thomas-Fermi potential $V_{\rm TF}(r,\lambda)$ with a scaling parameter λ, which can be determined by fitting calculated level energies to the experimental level energies.

The core polarization potential with non-negligible dipole and quadrupole contributions can be written as [14]

$$V_{\rm pol}(r,r_c) = -\frac{\alpha_d}{2r^4}[1 - e^{-(r/r_c)^6}] \tag{3}$$

$$-\frac{\alpha_q - 3\beta_q}{2r^6}[1 - e^{-(r/r_c)^{10}}]. \tag{4}$$

The values for the dipole α_d, and quadrupole α_q core polarizabilities as well as for the dynamic correction β_q were taken from [14]. r_c represents a cutoff radius that depends on the angular momentum l of the valence electron and that is chosen together with the scaling parameter λ in order to match the experimental energies for the lowest lying states, i.e., the $6S_{1/2}$, $6P_{1/2}$, $6P_{3/2}$, $5D_{3/2}$, and the $5D_{5/2}$ state.

The spin-orbit potential $V_{\rm so}(r)$ is written with a relativistic correction as

$$V_{\rm so}(r) = \frac{\alpha^2}{4}\frac{1}{r}\frac{dV'(r)}{dr}\frac{1}{\left[1 + \frac{1}{4}\alpha^2 V'(r)\right]^2}\vec{L}\cdot\vec{S}. \tag{5}$$

The potential in Eq. (5) is $V'(r) = V_{\rm TF}(r,\lambda) + V_{\rm pol}(r,r_c)$ and α is the fine structure constant. The total potential $V_{\rm Cs}(r)$ seen by the free Cs atom's valence electron can then be used in the radial Schrödinger equation

$$-\frac{1}{2}\frac{d^2u(r)}{dr^2} + \left[V_{\rm Cs}(r) + \frac{l(l+1)}{2r^2}\right]u(r) = Eu(r) \tag{6}$$

to obtain the wave functions and eigenenergies of the free Cs atom. The total wave function of the valence electron is written as a product of radial and angular parts $\Psi(\mathbf{r}) = Y_{l,m}(\vartheta,\varphi)u(r)/r$. The boundary condition near the core is (see, for example, [15])

$$u(r) \propto r^{l+1} \quad \text{for } r \to 0. \tag{7}$$

For $r \to \infty$ we use the condition that the wave function has an exponential decay. All numerical calculations were performed with MATHEMATICA 5.0. Figure 2 shows the calculated wave function for the ground and the first excited state of the free Cs atom. After having adjusted the parameters λ and r_c to yield the best agreement with experimental energies of the five lowest fine structure levels, the calculated energies of the states up to $n = 12$ were found to agree within 0.5% with their experimental values [16]. For higher lying states the values were compared to the values obtained using the hydrogen formula [17] with an effective principle quantum number n^* [16] and an agreement within 1% was obtained.

C. Cs-He interaction

The interaction of the Cs valence electron with the He atom $V_{\rm He}(\mathbf{r},\mathbf{R})$, is treated in a similar way as its interaction with the Cs core in terms of a potential

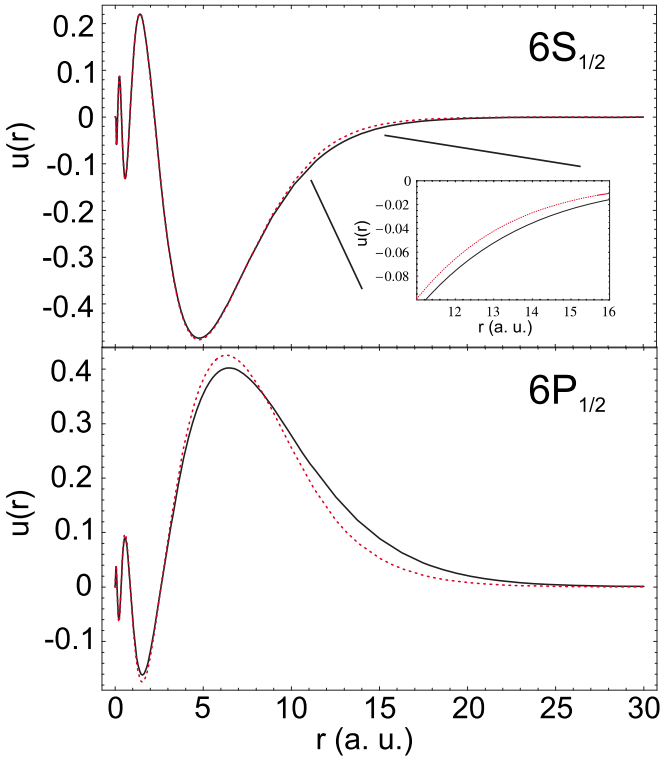

FIG. 2. (Color online) Calculated wave functions $u(r)$ for the $6S_{1/2}$ and the $6P_{1/2}$ states of Cs for the free Cs atom (black solid curve) and for the Cs in the bubble (red dashed curve). The bubble parameters are $\epsilon = 2.45 a_0^{-1}$ and $R_0 = 10.2 a_0$, which correspond to the equilibrium bubble of the Cs ground state in bcc solid He. The inset in the upper graph shows the main difference between the two wave functions at a distance $13a_0$ from the nucleus.

$$V_{\mathrm{He}}(\mathbf{r},\mathbf{R}) = V_{e\text{-He}}(\mathbf{r},\mathbf{R}) + V_{\mathrm{pol\ He}}(\mathbf{r},\mathbf{R}). \tag{8}$$

$V_{e\text{-He}}(\mathbf{r},\mathbf{R})$ [18] is a pseudopotential that models the repulsion of the Cs valence electron when it enters the electronic cloud of the He atom due to the Pauli principle—the main reason for the bubble formation—and the incomplete screening of the nuclear charge of the He atom. This pseudopotential can be written as

$$V_{e\text{-He}}(\mathbf{r},\mathbf{R}) = \sum_{l=0}^{\infty} \sum_{m=-l}^{l} V_l^{\mathrm{sr}}(r_{\mathrm{He}}) |Y_{lm}(\hat{r}_{\mathrm{He}})\rangle\langle Y_{lm}(\hat{r}_{\mathrm{He}})|, \tag{9}$$

in terms of a basis set of Gaussian potentials $V_l^{\mathrm{sr}}(r_{\mathrm{He}}) = C_l \exp(-D_l r_{\mathrm{He}}^2)$, centered on the He atom. The projection operators $|Y_{lm}(\hat{r}_{\mathrm{He}})\rangle\langle Y_{lm}(\hat{r}_{\mathrm{He}})|$ in Eq. (9) (l and m are the orbital momentum of the valence electron and its projection with respect to the He atom) are used to express the potentials with respect to coordinates centered on the Cs^+ core. The parameters C_l and D_l are taken from [18] and $\mathbf{r}_{\mathrm{He}} = \mathbf{r} - \mathbf{R}$.

The second term of Eq. (8) can be written in analogy to the polarization potential of the free Cs atom in Eq. (3) as [18]

$$V_{\mathrm{pol\ He}}(\mathbf{r},\mathbf{R}) = -\frac{1}{2}\frac{\alpha_{d\mathrm{He}}}{(r_{\mathrm{He}}^2 + r_{c\mathrm{He}}^2)^2} - \frac{1}{2}\frac{\alpha_{q\mathrm{He}} - 6\beta_{q\mathrm{He}} + 2\alpha_{d\mathrm{He}} r_{c\mathrm{He}}^2}{(r_{\mathrm{He}}^2 + r_{c\mathrm{He}}^2)^3}, \tag{10}$$

with the dipole polarizability $\alpha_{d\mathrm{He}}$, the quadrupole polarizability $\alpha_{q\mathrm{He}}$ and a dynamic correction parameter $\beta_{q\mathrm{He}}$. $V_{\mathrm{polHe}}(\mathbf{r},\mathbf{R})$ shows the asymptotic r^{-4} and the r^{-6} dependences of the dipole and quadrupole polarizabilities and is screened at small distances by the parameter $r_{c\mathrm{He}}$.

A further contribution comes from the core-core interaction

$$V_{\mathrm{cc}}(R) = V_{\mathrm{cc}}^{\mathrm{rep}}(R) - \frac{1}{2}\frac{\alpha_{d\mathrm{He}}}{(R^2 + r_{c\mathrm{He}}^2)^2} - \frac{1}{2}\frac{\alpha_{q\mathrm{He}} - 6\beta_{q\mathrm{He}} + 2\alpha_{d\mathrm{He}} r_{c\mathrm{He}}^2}{(R^2 + r_{c\mathrm{He}}^2)^3}, \tag{11}$$

which describes the polarization of the He atom by the Cs^+ ion, and where $V_{\mathrm{cc}}^{\mathrm{rep}}(R) = ae^{-bR}$ is a repulsive potential, acting at small distances, where the electronic clouds of the two atoms start to overlap.

Finally, we include a cross term $V_{\mathrm{cross}}(\mathbf{r},\mathbf{R})$, which represents the simultaneous polarization of the He atom by the Cs valence electron and the Cs^+ core

$$V_{\mathrm{cross}}(\mathbf{r},\mathbf{R}) = f_{\mathrm{cutoff}}(r,R)\left[-\frac{\alpha_{d\mathrm{He}}\cos\vartheta_{\mathrm{He}}}{(R^2 + r_{c\mathrm{He}}^2)(r_{\mathrm{He}}^2 + r_{c\mathrm{He}}^2)} + \frac{1}{2}\frac{\alpha'_{q\mathrm{He}}(3\cos^2\vartheta_{\mathrm{He}} - 1)}{(R^2 + r_{c\mathrm{He}}^2)^{3/2}(r_{\mathrm{He}}^2 + r_{c\mathrm{He}}^2)^{3/2}}\right], \tag{12}$$

with the definitions $\alpha'_{q\mathrm{He}} = \alpha_{q\mathrm{He}} - 6\beta_{q\mathrm{He}} + 2\alpha_{d\mathrm{He}} r_{c\mathrm{He}}^2$, ϑ_{He} being the angle between $\mathbf{r}$ and $\mathbf{R}$. This term is needed to yield the correct behavior at large internuclear distances. The cutoff function $f_{\mathrm{cutoff}}(r,R)$ is taken as

$$f_{\mathrm{cutoff}}(r,R) = \begin{cases} 1 - e^{-(R/r-1)^2}, & r \le R \\ 0, & r > R. \end{cases} \tag{13}$$

It assures that the cross term vanishes for small internuclear distances, where the electronic clouds overlap.

The parameter values used in the present calculations are taken from [18] and are listed in Table I, together with our values for the parameters for the free Cs atom, which differ slightly from the ones used in [14].

D. Integration over the bubble and the bubble energy

We have now a complete expression that determines the interaction of the Cs valence electron with a single He atom. In order to calculate the interaction with all the helium atoms surrounding the Cs atom we treat the latter as an empty bubble in an incompressible fluid with a spherically symmetric density distribution $\rho(\mathbf{R})$,

TABLE I. Numerical values of parameters used for the numerical evaluation.

	Value (unit)	Used in
α_d	19.03 (a_0^3)	$V_{\rm pol}(r,r_c)$
α_q	118.26 (a_0^5)	$V_{\rm pol}(r,r_c)$
β_q	19.18 (a_0^4)	$V_{\rm pol}(r,r_c)$
r_c (l=0)	3.2272 (a_0)	$V_{\rm pol}(r,r_c)$
r_c (l=1)	3.3.918 (a_0)	$V_{\rm pol}(r,r_c)$
λ	1.07623	$V_{\rm TF}(r,\lambda)$
$\alpha_{d\rm He}$	1.3834 (a_0^3)	$V_{\rm pol\ He}(\mathbf{r},\mathbf{R})$ and $V_{\rm cc}(R)$
$\alpha_{q\rm He}$	2.3265 (a_0^5)	$V_{\rm pol\ He}(\mathbf{r},\mathbf{R})$ and $V_{\rm cc}(R)$
$\beta_{q\rm He}$	0.706 (a_0^4)	$V_{\rm pol\ He}(\mathbf{r},\mathbf{R})$ and $V_{\rm cc}(R)$
$r_{c\rm He}(l=0)$	1 (a_0)	$V_{\rm pol\ He}(\mathbf{r},\mathbf{R})$, $V_{\rm cc}(R)$ and $V_{\rm cross}(\mathbf{r},\mathbf{R})$
a	49.1559	$V_{\rm cc}^{\rm rep}(R)$
b	1.8747 (a_0^{-1})	$V_{\rm cc}^{\rm rep}(R)$
C_l (l=0)	2.03	$V_l^{\rm sr}(r_{\rm He})$
D_l (l=0)	0.463 (a_0^{-2})	$V_l^{\rm sr}(r_{\rm He})$
C_l ($l\geqslant 0$)	−1	$V_l^{\rm sr}(r_{\rm He})$
D_l ($l\geqslant 0$)	1 (a_0^{-2})	$V_l^{\rm sr}(r_{\rm He})$

$$\rho(R,R_0,\epsilon)=\begin{cases}0, & R<R_0\\ \rho_0[1-\{1+\epsilon(R-R_0)\}e^{-\epsilon(R-R_0)}], & R\geqslant R_0,\end{cases} \tag{14}$$

where R_0 is the bubble radius. ϵ describes the steepness of the density distribution at the bubble interface and ρ_0 is the bulk density $\rho(R\gg R_0)$, which depends on the He temperature and pressure.

The energy needed to form a bubble is written in the commonly used way [8] as

$$E_{\rm bub}=\frac{4}{3}\pi R_b^3 p+4\pi R_b^2\sigma+E_{\rm kin}, \tag{15}$$

where p is the He pressure. The first term is the pressure volume work and the second term represents the energy of the surface tension. The third term is the volume kinetic energy due to the localization of the He atoms at the bubble interface. It is expressed as

$$E_{\rm kin}=\frac{h}{16\pi m_{\rm He}}\int d^3R\frac{(\nabla\rho(R,R_0,\epsilon))^2}{\rho(R,R_0,\epsilon)}, \tag{16}$$

where $m_{\rm He}$ is the mass of the He atom. The radius R_b used in Eq. (15) is the center of mass of the bubble interface defined by the equation

$$\int_0^{R_b}\rho(R,R_0,\epsilon)R^2dR=\int_{R_b}^{\infty}[\rho_0-\rho(R,R_0,\epsilon)]R^2dR. \tag{17}$$

In order to obtain electronic wave functions of the Cs atom confined in the bubble, we first integrate the potential over the He bulk

$$V_{\rm tot}^{\rm bub}(r,R_0,\epsilon)=V_{\rm Cs}(r)+\int d^3R\rho(R,R_0,\epsilon)[V_{\rm He}(\mathbf{r},\mathbf{R})+V_{\rm cross}(\mathbf{r},\mathbf{R})+V_{\rm cc}(R)], \tag{18}$$

and then solve the radial Schrödinger equation [Eq. (6)] by replacing $V_{\rm Cs}$ with $V_{\rm tot}^{\rm bub}$. The interaction of the Cs atom with an isolated He atom has no central symmetry. However, the integration over the bubble simplifies the problem since it leads to a central potential, so that the radial and angular variables can be separated.

The solutions depend on two parameters: R_0 and ϵ. In this way we do not only get the eigenenergy $E_{\rm int}$ depending on the bubble size but also the wave function of the valence electron $\Psi(r)=u(r)/r$. In Fig. 2 we compare the calculated radial wave functions for the $6S_{1/2}$ and the $6P_{1/2}$ states of the free Cs atom with those of a Cs atom in a spherical bubble. The wave functions of the atom in the bubble are slightly compressed by the bubble, the effect being more pronounced for the more extended $6P_{1/2}$ wave function.

The knowledge of the wave functions is important for the calculation of atomic properties such as transition dipole moments, excited state lifetimes, or hyperfine structure. The equilibrium size of the bubble is determined via a numerical minimization of the total energy $E_{\rm tot}^{\rm bub}$ of the system by varying R_0 and ϵ. The total energy is the sum of the bubble energy [Eq. (15)] and the interaction energy $E_{\rm int}$

$$E_{\rm tot}^{\rm bub}=E_{\rm int}+E_{\rm bub}. \tag{19}$$

The bubble parameters for both $6S_{1/2}$ and $6P_{1/2}$ states of Cs in bcc solid He close to liquid-solid phase boundary (p =26.9 bars, T=1.5 K) are compared with those calculated in [4] in Table II. For the surface tension coefficient σ we use

TABLE II. Comparison of our equilibrium bubble parameters with values from [4]. $\Delta E_{\rm exc}$ and $\Delta E_{\rm em}$ are the shifts of the excitation and emission lines, respectively, compared to the free atom. The values of this work are for a bcc crystal at T=1.5 K and p=26.9 bars. Values from [4] are for bcc at T=1.6 K and p =27.06 bar.

	R_0 (a_0)	ϵ ($1/a_0$)	R_b (a_0)	ΔE_S	ΔE_P	$\Delta E_{\rm exc}$ (cm^{-1})	$\Delta E_{\rm em}$ (cm^{-1})
$6S_{1/2}$ this work	10.22	2.45	11.06	186.8	780.6		
$6P_{1/2}$ this work	12.95	1.99	13.99	501.7	651.2	593.8	149.5
$6S_{1/2}$ from [4]	10.75	1.28	12.42	290.3	781.4		
$6P_{1/2}$ from [4]	13.08	1.12	14.97	418.3	539.4	491	121

its measured value (σ=0.332 dyne/cm) at T=1.5 K at saturated vapor pressure [19]. No experimental data on its pressure dependence are available, and we assume that it is independent of pressure as discussed in the literature on electron bubbles [20], where different models for the pressure dependence of σ are suggested. In the range of parameters studied in our work the surface energy produces a contribution of about $\approx$10% to $E_{\rm tot}^{\rm bub}$, so that our results are rather insensitive to variations of σ.

E. Hyperfine structure of Cs in solid He

As a first test of our model we have used the calculated $6S_{1/2}$ wave function to derive the bubble-induced change of the hyperfine coupling constant in the Cs ground state. The frequency of the corresponding hyperfine transition in bcc solid He has been measured earlier by our group [21]. It was found to be blueshifted by approximately 196 MHz with respect to the free transition in free atoms (9192 MHz), with a slight pressure dependence.

The matrix elements of the hyperfine (Fermi contact) Hamiltonian $H_{\rm hf}$ in the cesium ground state are

$$H_{\rm hf} = A_{\rm hf}\langle S,m_S,I,m_I|\mathbf{I}\cdot\mathbf{S}|S,m_S,I,m_I\rangle,$$

with

$$A_{\rm hf} = -\frac{2\mu_0}{3}\frac{\mu_B^2 g_I g_S}{\hbar^2}\langle n,L,m_L|\delta(\mathbf{r})|n,L,m_L\rangle, \qquad (20)$$

The matrix element in Eq. (20) depends on the value of the wave function at the nucleus.

$$A_{\rm hf} = -\frac{2\pi}{3}\alpha^2 g_I g_S |\Psi(0)|^2, \qquad (21)$$

and the hyperfine splitting of the ground state is $\delta\nu$=4$A_{\rm hf}$.

We first calculate the hyperfine splitting for the free Cs atom using the correction factors from [22] to account for relativistic effects and electrostatic and magnetic volume corrections. The obtained value ν=9770 MHz is approximately 6% larger than the experimental one. Our calculation of $\delta\nu$ for a Cs atom in a He bubble in the bcc phase shifts this value by 182 MHz to larger frequencies, which agrees within 6% with the experimentally measured shift of 196 MHz [21]. This increase of the hyperfine transition frequency is due to the compression of the electronic wave function by the surrounding pressurized He, which increases $|\Psi(0)|^2$.

F. Fine structure of Cs in solid He

The $6P_{1/2}$ and $6P_{3/2}$ fine structure doublet in the free Cs atom is split by 554 cm^{-1}. In condensed helium this splitting cannot be studied in emission since the $6P_{3/2}$ state is quenched by the formation of exciplexes and a strong mixing with the $6P_{1/2}$ state [7,9]. However, the transitions to both excited states can be studied via their absorption spectra.

The theoretical treatment of [4] neglects the effect of the He matrix on the fine structure splitting, although their experimental results show that the splitting increases with He pressure, reaching Δ=670 cm^{-1} at 20 bars. Our experimental results show a further increase up to Δ=700 cm^{-1} in hcp solid He at 30 bars [9]. The theoretical model presented above allows us to calculate this splitting as the difference between the eigenenergies of the perturbed $6P_{1/2}$ and $6P_{3/2}$ states in a spherical bubble formed around the ground state Cs atom. For liquid He at 25 bars we obtain Δ=642 cm^{-1} and for bcc solid Δ=649 cm^{-1}. In both cases the splitting is underestimated, however, the sign of the shift and its order of magnitude are predicted correctly. The theoretical model used in this work is refined with respect to the one of [4] as it takes the bubble effect on the fine-structure splitting into account.

G. Lifetime of the $6P_{1/2}$ state

With the theoretical model presented above we also calculate the lifetime τ of the excited $6P_{1/2}$ state of Cs in condensed He. Experimental data on the dependence of τ on He pressure are available for superfluid He [23] up to the solidification point. Recently we have measured lifetimes in bcc and hcp solid He up to p=36 bars [24]. The results of [23,24] show that in liquid and bcc solid He, τ has a pressure independent value of 32.5 ns, 2.3 ns shorter than the lifetime in a free Cs atom. At the phase transition to the hcp phase the lifetime shortens by 3.2 ns and further decreases with increasing He pressure.

The radiative lifetime τ of an excited state is related to the transition dipole moment $|\langle 6P_{1/2}\|er\|6S_{1/2}\rangle|$ and frequency ω_0 via

$$\frac{1}{\tau} = \frac{\omega_0^3 e^2}{3\pi\epsilon_0\hbar c^3}\frac{1}{2}|\langle 6P_{1/2}\|r\|6S_{1/2}\rangle|^2. \qquad (22)$$

We have calculated the transition dipole moment using the wave functions of the $6P_{1/2}$ and $6S_{1/2}$ states of Cs perturbed by the bubble, as discussed in detail in [24]. The results show that the dipole moment decreases with increasing pressure. However, this change is largely compensated by a simultaneous increase of the transition frequency (the blueshift discussed in the following subsection) and the resulting lifetime is almost constant in agreement with the experimental data in liquid and bcc solid He. We have also shown [24] that the reduction of τ with respect to its free atomic value is due to the interaction of the atomic dipole with its own radiation field reflected at the bubble interface (cavity effect). In the case of hcp matrices the observed pressure dependence of τ is attributed to the onset of a pressure-dependent radiationless formation of exciplex [24].

H. Cavity effect

The above treatment has not yet taken into account that the excited Cs atom interacts with its own electromagnetic radiation reflected at the bubble interface. It is well known that a static (or oscillating) electric dipole close to a dielectric interface induces a static (or oscillating) polarization in the dielectric. The interaction between the dipole and its mirror image in the dielectric results in a redshift of the emitted light, and affects the lifetime of the atomic oscillator [24]. The problem of an excited atom interacting with a spherical

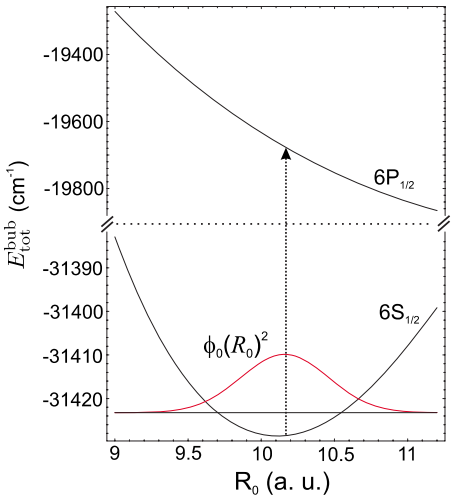

FIG. 3. (Color online) Calculated potential energy (solid black line) of the Cs $6S_{1/2}$ ground state in the spherical bubble including the bubble energy as a function of the bubble radius R_0 with the probability distribution $\phi_0(R_0)^2$ shown as a red curve.

microcavity in a dielectric has been treated in [25]. The shift of the transition frequency is given by

$$\delta = -\frac{e^2}{2\omega_0 m_0 d^2}\mathrm{Re}[\mathbf{d}\cdot\mathbf{E}], \tag{23}$$

where m_0 is the electron mass, ω_0 is the transition frequency, $\mathbf{d}$ is the transition dipole moment, and $\mathbf{E}$ is the field produced by the polarized dielectric at the position of the atom. We have evaluated this expression and calculated the corresponding correction to the transition frequency. For a given bubble configuration we made a numerical evaluation of the induced polarization in the surrounding solid He and calculated the field produced by that polarization at the center of the bubble. Retardation effects can be neglected because of the small bubble size. For bcc solid He at 1.6 K we obtain a redshift of 44 cm^{-1} for the emission line and of 83 cm^{-1} for the absorption line. This cavity effect is taken into account in the calculated lineshifts presented in Fig. 5. The same approach was used in [26] to calculate wavelength corrections of the absorption line of alkali atoms (Li, Na, K) bound in a dimple at the surface of He nano droplets. In that case the correction was much smaller, about 9 cm^{-1}, due to the loosely bound structure of the trapping site.

I. Line shape of absorption and emission lines

A standard way [27] for calculating the line shape of the $6S_{1/2}$-$6P_{1/2}$ absorption line consists in considering the smearing out of the ground state wave function due to bubble oscillations. Here we consider only radial (breathing mode) oscillations around the equilibrium bubble radius $R_0(6S)$, whose wave function can be obtained in the following way. Figure 3 shows the total bubble energy $E_{\mathrm{tot}}^{\mathrm{bub}}$ as a function of the bubble radius. We use this energy (and not just its harmonic approximation near the minimum) as the potential in a one-dimensional Schrödinger equation. The solutions then yield the eigenenergies and wavefunctions of the oscillations.

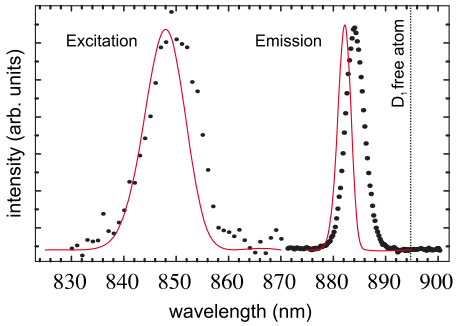

FIG. 4. (Color online) Experimental (black dots) and theoretical (solid red line) excitation and emission spectrum of the $6S_{1/2}-6P_{1/2}$ transition in the bcc phase of solid He. Experimental conditions: $T\simeq 1.6$ K, $p=27.8$ bars. Note the good agreement of the line positions within the experimental linewidths. The line positions as a function of He pressure are shown in Fig. 5.

We consider the mass of the oscillator to be the hydrodynamic mass of the bubble $M_{\mathrm{eff}}=4\pi {R_b}^3\rho_0 m_{\mathrm{He}}$.

The splitting between the vibrational ground state and the first excited vibrational level is equivalent to 7.5 K at 26.6 bar, so that at the temperature $T=1.6$ K of the experiment, only the lowest vibrational state is populated. The probability distribution for finding a bubble with radius R_0 is then given by $|\phi_0(R_0)|^2$, where $\phi_0(R_0)$ is the wave function associated with the corresponding zero-point energy, whose R_0 dependence is shown in Fig. 3. To each bubble radius R_0 corresponds a given transition energy with a relative weight given by $|\phi_0(R_0)|^2$. An equivalent procedure can be applied for calculating the emission spectra. In that case one starts from breathing mode oscillations of the bubble around $R_0(6P)$.

The shape and the size of the bubble do not change during the electronic transition since the transition occurs on a time scale shorter than the bubble oscillation period (Frank-Condon principle). Once the Cs atom is excited the bubble relaxes to a larger radius that reflects the larger extension of the excited state wave function. One can estimate that this relaxation occurs on a picosecond time scale. The fluorescence transition occurs in the larger bubble in which the excited state lives for a few ten ns, close to the free atomic lifetime.

In Fig. 4 we compare the theoretical excitation and emission line shapes for the D_1 ($6S_{1/2}$-$6P_{1/2}$) line in a bcc He crystal to the experimentally measured spectra. Both absorption and emission lines are blueshifted and broadened with respect to the free atomic line. The repulsive interaction between the valence electron and the bubble interface shifts both atomic states towards higher energies. Since the electronic wave function of the excited state has a larger radial extension the shift of that state is larger. As a result the net transition energy increases and the lines become blueshifted. The shift and broadening are more pronounced in absorption since it occurs in a bubble of smaller size than the bubble in which the emission occurs. The calculated transition wavelengths, defined as the numerically evaluated centers of gravity of the lines are shown as a function of He pressure in Fig. 5 together with experimental results for pressures ranging

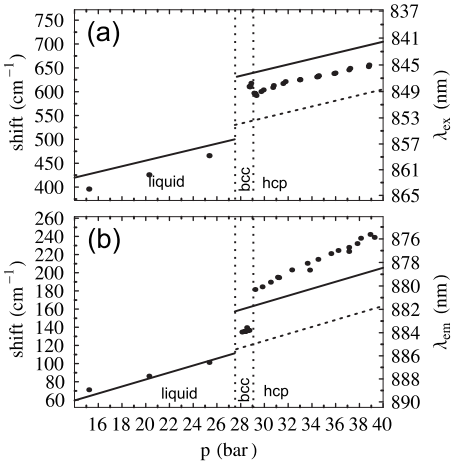

FIG. 5. Experimental (dots) excitation (a) and emission (b) wavelengths of the $6S_{1/2} \rightarrow 6P_{1/2}$ (D_1) transition. Experimental data in liquid He are taken from [4]. The solid lines are calculated using the extended SBM presented in this work (the extension of the model is discussed in Sec. IV A) including the cavity shift. The dashed lines show the predicted jumps at the liquid-solid phase transition without using the extended model (only SBM). Vertical dashed lines mark the phase transitions of condensed He.

from liquid He (He II), via the crystalline bcc phase to the hcp phase. As a general trend the transition frequencies increase with increasing He pressure due to the increased perturbation of the Cs atom by the He matrix.

III. EXPERIMENT

The experiments were performed in a Cs doped solid He matrix. Details of the technique for doping a He crystal were presented in previous publications [28,29]. A He crystal is produced by pressurizing liquid He in a copper cell immersed in a liquid He bath cooled to 1.6 K by pumping on its surface. The cell has five windows in three orthogonal directions for optical access. The crystal is doped with Cs atoms by laser ablation using a frequency doubled pulsed Nd:YAG laser (532 nm, repetition rate ~3 Hz, pulse energy 10 mJ). The laser beam is focused by a height adjustable lens mounted above the cell onto a solid Cs target located at the bottom of the cell. A cw diode laser at 850 nm, or the idler output of a tunable optical parametric oscillator (OPO) pumped by the third harmonic of a Nd:YAG laser were used for the optical excitation of the implanted atoms. The idler beams of the OPO can be tuned over the range 770−1100 nm. The atomic fluorescence light is collected by a lens inside the cryostat and collimated into a direction perpendicular to the ablation and excitation laser beams, where it is focused into a grating spectrograph (MS257, Oriel) equipped with a CCD camera. All measurements were done at 1.5 or 1.6 K, in the pressure range of 26−38 bars, either in the bcc or hcp phase of solid He.

Excitation spectra. The excitation spectrum of the D_1 transition recorded in the bcc phase at 27 bars is shown in Fig. 4. This spectrum was obtained by tuning the OPO over the range of 820−870 nm in 1 nm steps, while recording the emitted fluorescence near 880 nm. The measurements were repeated for different helium pressures. At each pressure the center of gravity of the excitation band was determined numerically. The dependence of the line centers λ_{ex} as a function of He pressure are shown in Fig. 5(a), where they are compared to the theoretical predictions.

The experimental pressure dependence of the absorption (and emission) lines presented in Fig. 5 can be compared to corresponding measurements in pressurized superfluid He [4] shown in the same plot. In He II the absorption line shows an almost linear shift towards shorter wavelengths with increasing He pressure, and the data in solid He have a pressure shift with a practically identical slope. This common slope is very well predicted by the SBM calculations made in this work (solid lines in Fig. 5).

A prominent feature in Fig. 5 is the large jump δ_{ex} of the excitation wavelength at the boundary between the liquid and solid phases. At the liquid-bcc phase transition the He density ρ_0 increases by about 8%. In the bubble model this change of density yields a blueshift of the excitation line by approximately 2 nm (28 cm^{-1}), much smaller than the experimentally observed jump of 10 nm (140 cm−1). The excitation line shows another jump—of opposite sign—at the bcc-hcp phase transition. At this point the helium density increases by 0.4%, for which the SBM predicts a blueshift of 0.2 nm (3 cm^{-1}), not visible on the scale of Fig. 5, whereas the measured λ_{ex} shifts by 1.5 nm (20 cm^{-1}) to the red. We interpret the sign and magnitude of this jump as being due to the static quadrupolar deformation of the atomic bubble in the uniaxial hcp crystal [29]. Clearly, the bubble model assuming spherical bubble shapes is not capable of treating this phenomenon and the development of an extended bubble model that takes bubble deformations into account is in progress.

Emission spectra. We have also measured the pressure dependence of the D_1 emission line center λ_{em} excited at a fixed wavelength (850 nm). The excitation wavelength was not adjusted when changing the pressure since the absorption line is rather broad (Fig. 4). The results are shown in Fig. 5(b), where the positions of the emission lines are taken as their centers of gravity.

The pressure shift of the emission line λ_{em} [Fig. 5(b)] also shows a linear dependence on He pressure. However, the slope is now different in the liquid and solid phases. The spherical bubble model gives a very good agreement with the slope and the absolute values in liquid He and slightly underestimates the one in solid He. As in the case of the absorption line, the blue jump δ_{em}=2 nm (30 cm^{-1}) observed at the He II-bcc transition cannot be explained by the spherical bubble model as being due to the 8% increase of density. Another remarkable fact is that the jump of the emission line at the bcc-hcp phase transition is towards shorter wavelengths. The SBM predicts the same sign of the jump, but strongly underestimates its magnitude.

IV. DISCUSSION

A. Extension of the bubble model

The calculations using the spherical bubble model presented here as well as those reported in [4] cannot reproduce

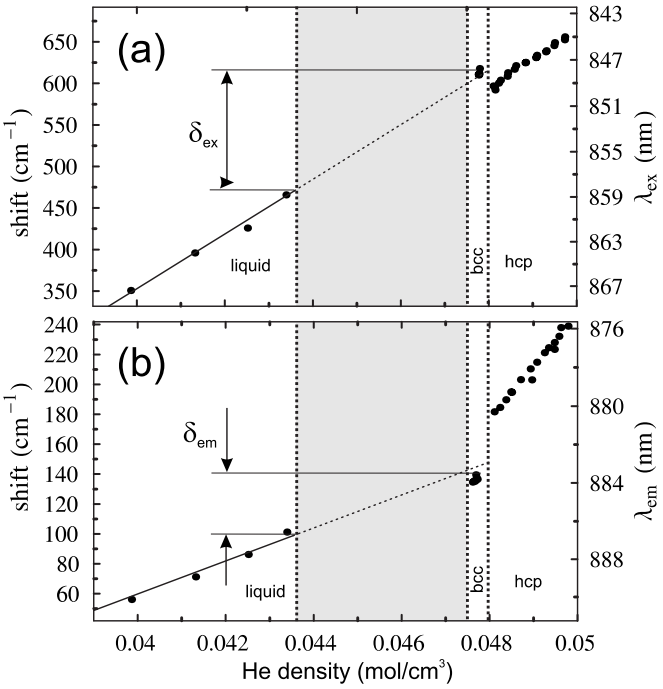

FIG. 6. Experimental excitation (a) and emission (b) wavelengths (dots) of the D_1 line as a function of the He density. Data in liquid He are taken from [4]. The solid lines are fits to the data in the liquid phase. Vertical dotted lines mark phase boundaries. The gray region represents the experimentally nonaccessible densities corresponding to the density jump at the liquid-bcc transition.

the large jump of the excitation and emission lines at the liquid-solid phase transition observed in the experiments. In this subsection we suggest an extension of the SBM which explains this experimental observation.

In Fig. 6 λ_{ex} and λ_{em} (the same data as in Fig. 5) are plotted as functions of the He density ρ rather than of the He pressure. Both density dependencies are linear since in liquid and solid He the density is nearly proportional to the pressure (except for the discontinuity at the phase boundary). The striking feature of Fig. 6 is that the data points measured in the bcc phase and those in liquid He lie exactly on the same straight line, without any jump at the phase boundary. This observation suggests that it is the density rather than the pressure, which is responsible for the "pressure" shift. At the same time, the shift at the bcc-hcp phase boundary has a different nature and is most likely related to the change in the bubble shape due to the anisotropy of the crystal.

In liquid He the equilibrium bubble radius R_0 is established as a balance between the repulsive Cs-He interaction (discussed in Sec. II C) and the bubble energy E_{bub}, which is minimized for $R_0 \to 0$ [Eq. (15)]. The former is proportional to the He density ρ [see Eq. (18)], while the latter is dominated by the pV term and is thus proportional to the He pressure. An increase of the He pressure is accompanied by a corresponding increase of the He density and both E_{bub} and E_{int} increase. Therefore the total energy increases with a very small change (decrease) of the bubble radius. At the phase boundary the density increases by 8% without any change in the pressure. According to the SBM a new equilibrium bubble with a larger value of R_0 is established with a relatively small corresponding increase in energy. The undisturbed linear dependence of Fig. 6 suggests that the bubble stays frozen or even shrinks at the phase transition due to an additional force, which compensates the increased Cs-He repulsive force.

We identify this new force as an elastic restoring force, which appears in the solid compressed by the expansion of the bubble at *constant volume* of the sample. It is not present in liquid He, where the formation of the bubble proceeds by a displacement of helium at *constant pressure*. In order to calculate this restoring force we use the fact that in equilibrium it compensates the force acting on the bubble interface from inside.

$$F_{\text{elastic}} = -F_{\text{Cs-He}} = -\left.\frac{\partial E_{\text{int}}}{\partial R_0}\right|_{R_0=R_{\text{eq}}}, \tag{24}$$

where R_{eq} is the equilibrium bubble radius for a given electronic state (here $6S_{1/2}$ or $6P_{1/2}$). The energy of the deformation is then given by $F_{\text{elastic}}\Delta R$, where $\Delta R = R_0^{\text{solid}} - R_0^{\text{liquid}}$ is the difference between the equilibrium bubble size in solid and in liquid He. Equation (15) defining the bubble energy becomes

$$E_{\text{bub}} = \frac{4}{3}\pi R_b^3 p + 4\pi R_b^2 \sigma + E_{\text{kin}} - \left.\frac{\partial E_{\text{int}}}{\partial R_0}\right|_{R_0=R_0^{\text{liquid}}} \Delta R. \tag{25}$$

The additional term leads to an equilibrium bubble size in bcc He, which is slightly smaller than the bubble size in liquid. We have recalculated the spectra using the extended expression (25) for E_{bub}. The resulting pressure dependencies of the excitation and emission wavelengths are shown in Fig. 5 by solid lines. In both cases we obtain a much better agreement with the experimental results in He II and in bcc solid He than with the standard spherical bubble model (shown by dashed lines in Fig. 5).

The jump of excitation and emission lines at the bcc-hcp phase transition remains when plotted against density and cannot be explained, even in the frame of the present extension of the standard bubble model. The fundamental difference between the bcc and the hcp phases is the crystalline symmetry: the uniaxial hexagonal phase has strongly anisotropic elastic constants, which affect the shape of the atomic bubble. In consequence the potential seen by the valence electron is no longer a central potential. Some aspects of static anisotropic bubble deformations are discussed in [29]. A more detailed calculation of this effect on atomic spectra is currently underway and will be presented in a forthcoming publication.

B. Summary

We have presented a detailed discussion of the spherical bubble model for Cs atoms in liquid and solid ^{4}He with an important extension of the model that allows us to explain the sudden jumps of absorption and emission wavelengths of the Cs $6S_{1/2}$-$6P_{1/2}$ transition at the liquid-solid phase transition. The extension of the model includes an additional bubble energy term for the solid phase that accounts for the

elastic properties of the crystal and we included an additional shift due to the interaction of the excited Cs atom with its own radiation field (cavity effect). The extended bubble model gives an excellent agreement within the experimental linewidths of the absorption and emission wavelengths of Cs atoms in liquid and solid bcc He. We have shown that it is the density of the He matrix rather than its pressure that is responsible for the line shifts. The model calculations were also applied to measurements of the lifetime of the Cs $6P_{1/2}$ state [24], the fine structure and the hyperfine splitting in the Cs ground state and gave good agreement with experimental results. A model for the deformations of the atomic bubbles in the uniaxial hcp phase of solid He is in progress and will be the subject of a future publication.

ACKNOWLEDGMENTS

This work was supported by Grant No. 200021-111941/1 of the Schweizerischer Nationalfonds.

[1] C. C. Grimes and G. Adams, Phys. Rev. B **45**, 2305 (1992).
[2] A. Y. Parshin and S. V. Pereverzev, JETP **74**, 68 (1992).
[3] A. I. Golov and L. P. Mezhov-Deglin, JETP Lett. **56**, 514 (1992).
[4] T. Kinoshita, K. Fukuda, Y. Takahashi, and T. Yabuzaki, Phys. Rev. A **52**, 2707 (1995).
[5] T. Kinoshita, K. Fukuda, and T. Yabuzaki, Phys. Rev. B **54**, 6600 (1996).
[6] S. Kanorsky, A. Weis, M. Arndt, R. Dziewior, and T. Hänsch, Z. Phys. B: Condens. Matter **98**, 371 (1995).
[7] S. I. Kanorsky, M. Arndt, R. Dziewior, A. Weis, and T. W. Hänsch, Phys. Rev. B **49**, 3645 (1994).
[8] S. I. Kanorsky, M. Arndt, R. Dziewior, A. Weis, and T. W. Hänsch, Phys. Rev. B **50**, 6296 (1994).
[9] P. Moroshkin, A. Hofer, D. Nettels, S. Ulzega, and A. Weis, J. Chem. Phys. **124**, 024511 (2006).
[10] J. Pascale and J. Vandeplanque, J. Chem. Phys. **60**, 2278 (1974).
[11] G. Peach, J. Phys. B **11**, 2107 (1978).
[12] P. Gombas, *Pseudopotentiale* (Springer-Verlag, Berlin-Gottingen-Heidelberg, 1956).
[13] B. H. Bransden and C. J. Joachain, *Physics of Atoms and Molecules* (Longman, London, New York, 1983).
[14] D. W. Norcross, Phys. Rev. A **7**, 606 (1973).
[15] C. Cohen-Tannoudji, *Quantum Mechanics* (Hermann, Paris 1977), Vol. 1.
[16] K. H. Weber and C. J. Sansonetti, Phys. Rev. A **35**, 4650 (1987).
[17] I. I. Sobelman, *Atomic Spectra and Radiative Transitions*, Springer series on Atoms and Plasmas (Springer, New York, 1992).
[18] J. Pascale, Phys. Rev. A **28**, 632 (1983).
[19] M. Iino, M. Suzuki, and A. J. Ikushima, J. Low Temp. Phys. **61**, 155 (1985).
[20] M. Rosenblit and J. Jortner, J. Phys. Chem. A **101**, 751 (1997).
[21] S. Lang, S. Kanorski, M. Arndt, S. B. Ross, T. W. Hänsch, and A. Weis, Europhys. Lett. **30**, 233 (1995).
[22] H. Kopfermann, *Kernmomente* (Akademische Verlagsgemeinschaft G.M.H, Frankfurt am Main, 1956).
[23] T. Kinoshita, K. Fukuda, T. Matsuura, and T. Yabuzaki, Phys. Rev. A **53**, 4054 (1996).
[24] A. Hofer, P. Moroshkin, S. Ulzega, and A. Wei (unpublished).
[25] V. V. imov, M. Ducloy, and V. S. Letokhov, J. Mod. Opt. **43**, 549 (1996).
[26] F. Stienkemeier, J. Higgins, C. Callegari, S. I. Kanorsky, W. E. Ernst, and C. Scoles, Z. Phys. D: At., Mol. Clusters **38**, 253 (1996).
[27] S. Kanorsky and A. Weis, in *Quantum Optics of Confined Systems*, edited by M. Ducloy and D. Bloch (Kluwer Academic, Dortrecht, 1996), Vol. 314.
[28] M. Arndt, R. Dziewior, S. Kanorsky, A. Weis, and T. Hänsch, Z. Phys. B: Condens. Matter **98**, 377 (1995).
[29] P. Moroshkin, A. Hofer, S. Ulzega, and A. Weis, Fiz. Nizk. Temp. **32**, 1297 (2006) [Low Temp. Phys. **32**, 981 (2006)].